Modeling Earth Systems and Environment
https://doi.org/10.1007/s40808-021-01275-5

ORIGINAL ARTICLE

Integrated geophysical methods for delineating crustal structures and hydrothermal alteration zones for mineral exploration projects in parts of west-central, Nigeria

Leke Sunday Adebiyi[1,2] · Akinola Bolaji Eluwole[2] · Akindeji Opeyemi Fajana[2] · Naheem Banji Salawu[2,3] · Sesan Cornelius Falade[1] · Kehinde Oladele Dopamu[1] · Esther Adetola Alejolowo[1]

Received: 28 June 2021 / Accepted: 27 August 2021

Abstract

The knowledge that quite many primary deposits of economic minerals in Nigeria are structurally controlled, the principal of which are faults, folds, shear zones, mylonites and hydrothermal alteration zones among others, has informed the choice of this study. Although significant success has been recorded in mapping many of the recognized structures, there are yet many gaps to fill especially in the area of hydrothermal alteration mappings. To provide new insights for mapping alteration zones, the present study integrated two airborne geophysical methods namely magnetic and radiometric methods with ground geophysical surveys comprising the electrical resistivity tomography (ERT) and very-low-frequency electromagnetic (VLF-EM) methods. The airborne data were interpreted using standard geophysical techniques such as horizontal gradient magnitude, radiometric ratio and radiogenic heat production. The results obtained in each case showed that the hydrothermal zone H3, out of the six suspected hydrothermal alteration zones namely H1, H2, H3, H4 H5 and H6, has positive prospects for hydrothermal alteration zone. The length and the average width of 30 km and 5 km respectively of the alteration zone H3 enabled its detection from airborne surveys. The zone H3 was, thereafter, investigated with ERT and VLF-EM methods. The results obtained from the ERT showed a fairly deformed homogeneous layer of high electrical resistivity below fairly weathered heterogeneous formations. The result of the VLF-EM method, on the other hand, showed several weak zones suspected to be fracture zones that may have aided the circulation of the hydrothermal fluids for subsequent mineral precipitation in wall rocks.

Keywords Radiometric method · Magnetic method · Radiogenic heat · Hydrothermal alteration

Introduction

Hydrothermal alteration is a complex process involving the interaction of aqueous hot fluids with rocks leading to textural, mineralogical and chemical changes within the rocks through which the fluids circulate (Airo 2002; Smith and Davies 2006; Pirajno 1992; Lentz 1994; Lambert and Sato 1974; Thompson and Thompson 1996). The parts of the crust where such alteration process occurred is regarded as hydrothermal alteration zones. Notably, the style and pattern of hydrothermal alteration depend on the temperature, pressure and composition of the hydrothermal fluids, and by extension the nature and composition of the rock through which the fluids circulate (White et al. 2003; Airo 2002; Smith and Davies 2006; Eilu et al. 1999; Pirajno 1992; Lambert and Sato 1974; Meyer and Hemley 1967; Guilbert and Park 1986; Burnham 1981). Experimental results and thermodynamics description of the hydrothermal fluids formation from upwelling magma, including the minerals recrystallization in wall rocks by the infiltrating aqueous hydrothermal fluids, have been discussed in detail by Burnham (1979), Burnham (1997), Holland (1972), Burnham and Ohmoto (1980) and Mielke et al. (2014) among others. Hydrothermal alteration zones are very important in exploration geophysics because they allow exploration of ore

✉ Leke Sunday Adebiyi
adebiyi.leke@lmu.edu.ng; olalakes2012@gmail.com

[1] Department of Physical Sciences, Landmark University, PMB 1001, Omu-Aran, Kwara State, Nigeria

[2] Department of Geophysics, Federal University, Oye Ekiti, Oye-Ekiti, Ekiti State, Nigeria

[3] BS Geophysical and Consultancy Ltd, Ilorin, Nigeria

Published online: 13 September 2021

minerals to concentrate on small targets (Eldosouky et al. 2017; Airo 2002; Holden et al. 2011; Thompson and Thompson 1996; Pirajno 1992). To map alteration zones, geophysicists rely on the magnetic and radiometric anomalies that result from the alteration process. The magnetic method targets mainly geological formations characterized by low amplitude magnetic anomalies. This is because hydrothermal fluid caused magnetic minerals in rocks through which they circulate to lose their magnetic property and in the process become permanently demagnetized (Gunn and Milligan 1997; Dentith and Mudge 2014). The radiometric method, on the other hand, targets demagnetized geological formations exhibiting potassium enrichment and thorium depletion at places (Lawal 2020; Ohioma et al. 2017). These methods of diagnosing alteration zones have yielded fairly good results, and in some cases, lead to the discovery of primary ore deposits, especially in tropical Africa where weathering greatly affect the physical identification of alteration formations (Ohioma et al. 2017; Pirajno 1992). However, many similar but non-hydrothermal alteration zones such as those resulting from the migration of radioelements are, sometimes, delineated as hydrothermal alteration zones. The present study, therefore, represents an attempt to distinguish alteration zones from many similar but non-hydrothermal alteration zones. The study will interpret high-resolution aeromagnetic data of the target area for possible demagnetized zones. The aeroradiometric data of the same coverage will be processed to identify potassium enrichment and thorium depletion associated with suspected demagnetized zones. The radiogenic heat distribution for the entire area will be used to further narrow down the targets. Finally, two ground geophysical surveys namely electrical resistivity tomography and very-low-frequency electromagnetic methods will be deployed to investigate the mineral prospect of the final target(s).

Location and geologic setting

The study area is located in the west-central half of Nigeria and is underlain by the Precambrian basement complex of Nigeria. It extends from longitude 4° 30′ 00″ E to 5° 00′ 00″ E, and latitude 8° 00' 00" to 8° 30' 00' and occupies about 12,100 km^2. The basement complex of Nigeria is generally made up of the migmatite-gneiss complex, metasediment and metavolcanic rocks, older granitoid of the Pan-African orogeny, post-Pan-African granitic intrusions, and fragments of silicified quartzite-schist belt that tightly folded into the basement and consistent with the northeast-southwest geological strike. The crystalline basement rocks of the study area display a poly-orogenic sequence of reworked Archaean migmatite gneisses complex comprising mainly granite gneiss, migmatite, medium to coarse-grained biotite and hornblende-granite, and minor fine-grained flaggy quartz-biotite-gneiss, porphyritic granite, undifferentiated schist, banded gneiss, quartz-schist, and fine-grained biotite-granite (Fig. 1). It is part of the Precambrian basement complex that lies within the Trans-Sahara mobile belt between the West African Craton; the Gabon-Congo Craton and the Sahara meta-craton within the framework of the late Proterozoic and early Paleozoic Gondwana amalgam (Ajibade et al. 1987; Dada 2008; Salawu et al. 2020; NGSA 2006). The undifferentiated schist occupies mainly the south-southeastern part of the study area and extends northward through the eastern part. It is intruded by pegmatite dykes (P) which is generally discordant with the structural grain of the host formation. The banded gneiss occupies three locations namely the north, central, south-southwest and the western parts of the study area. Similarly, the north-northwest and parts of the north-northeastern study area are predominantly underlain by porphyritic granite (Fig. 1).

Data and methods

Data

Aeromagnetic data

The high-resolution aeromagnetic data in this study extend from longitude 40° 30′ E to 5° 00′ E and latitude 8° 00′ N to 8° 30′ N and covered about 12,100 km^2 on land. The data are part of the nationwide high-resolution airborne data acquired by Fugro Airborne Surveys on behalf of Nigeria in a series of NW–SE trends (NGSA 2007). The flight line and tie-line spacing for the data acquisition were 500 m and 2000 m respectively at a regular barometric flight height of about 80 m. Standard corrections including removal of international geomagnetic reference field (IGRF) from the magnetic data were implemented by Fugro Airborne Surveys.

Aeroradiometric data

Radiometric data in this study also extend from longitude 40° 30′ E–5° 00′E and latitude 8° 00′ N–8° 30′ N and covered about 12,100 km^2 on land. It is part of the airborne radiometric data acquired at the time of the aeromagnetic data acquisition. The data were acquired by mounting a high precision gamma-ray spectrometer with the aircraft that also carried a proton-precision magnetometer (NGSA 2007). The original data were corrected for background radiation and other necessary corrections by Fugro Airborne Surveys Company.

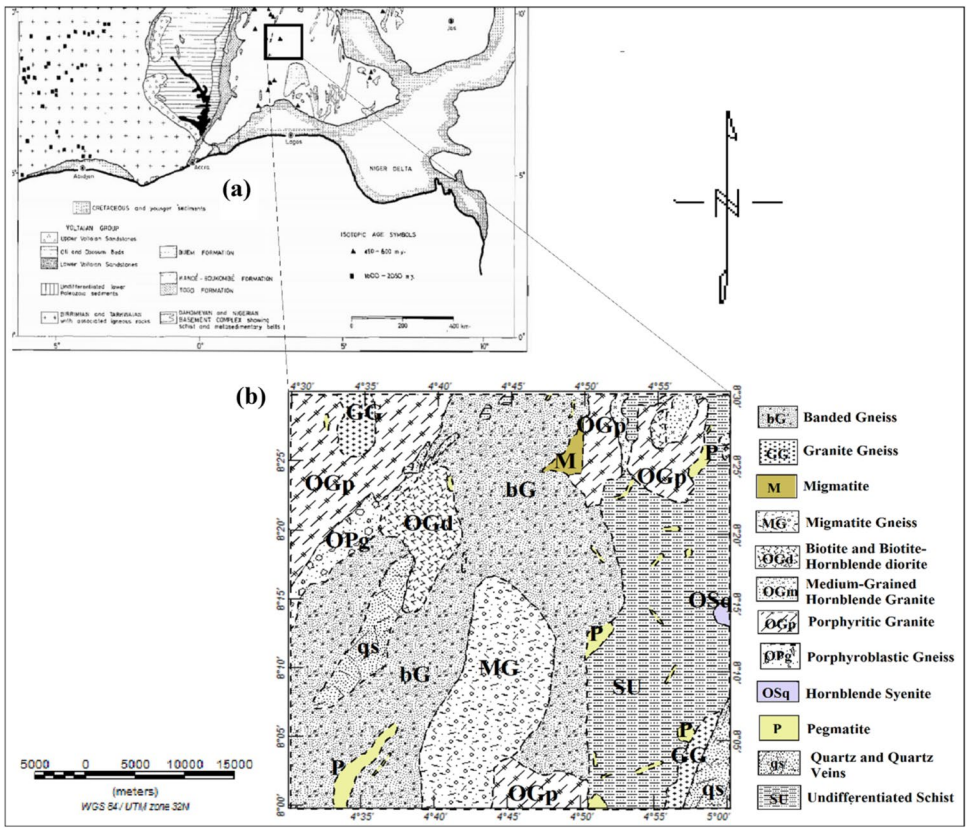

Fig. 1 **a** Simplified geology map of Nigeria and environ showing the study location (Thieblemont 2016; Salawu et al. 2020). **b** Geology map of the study area (NGSA 2006)

Magnetic methods

Reduction to the magnetic equator

Reduction to the magnetic equator (RTE) is a filter used to center the maxima and gradients of magnetic anomalies over their sources. It is applied to magnetic data acquired mainly in the low latitude magnetic hemisphere (Nabighian et al. 2005; Verduzco et al. 2004). Application of reduction to the magnetic pole (RTP) filter to the low latitude magnetic data often result in an excessive distortion of the original data (Nabighian et al. 2005; MacLeod et al. 1993; Salawu et al. 2019). The RTE transformation, though, very stable for low latitude magnetic data, it is not without its limitations. Interpreting the shapes of the magnetic structures of a reduced to the magnetic equator gridded data is difficult as a result of the dipole nature of magnetic anomalies (Nabighian et al. 2005; Salawu et al. 2019). Similarly, the RTE phase shift somewhat stretches anomalies in the east–west direction and suppresses the north-trending subtle anomalies (Blakely 1995; Salawu et al. 2019).

Horizontal gradient magnitude

Horizontal gradient magnitude (HGM) is the magnitude of the first-order horizontal derivatives of a potential field (Cordell and Grauch 1982). Equation 1 is the expression for HGM interpretation. The magnetic data to interpret should have been corrected for diurnal variation, international geomagnetic reference field (IGRF).

$$|\mathrm{HGM}(x,y)| = \sqrt{\left(\frac{\partial F}{\partial x}\right)^2 + \left(\frac{\partial F}{\partial y}\right)^2}. \quad (1)$$

The gradients $\frac{\partial F}{\partial x}$ and $\frac{\partial F}{\partial y}$ are the first-order partial derivatives of the residual magnetic intensity field, F in x and y horizontal directions respectively (Cordell and Grauch 1982). The method is used, generally, to detect linear structures such as contacts and faults from potential field data. This is based on the assumptions that the magnetic field and source magnetization are vertical; the contact is vertical and; sources are thick (Philips 2000). To satisfy the first two assumptions, it is necessary to apply a standard phase shift to the data known as a reduction to the equator for low latitude magnetic data or to pole for high latitude magnetic data using a Fourier transform filter. Provided that the assumptions are satisfied, the method is effective for mapping the boundary of magnetic source bodies and magnetic lineaments that may correspond to basement faults and contacts. The HGM method is less susceptible to noise in the data (Moritz 2009; Fedi and

Florio 2001; Adebiyi et al. 2020) and, therefore, very reliable for interpreting low latitude magnetic data, especially, the equatorial data.

Radiometric methods

Radiometric ratios

The relative concentration of radioelements in a given formation can be used as a benchmark for identifying different lithotypes and for identifying areas of preferential radioelement enrichment or depletion for mapping alteration zones and minerals precipitated in faults (Dentith and Mudge 2014). Generally, the radiometric measurements are affected by overburden thickness, vegetation cover, and soil moisture, while weathering decreases alteration signatures (Dickson and Scott 1997). The ratio of radiometric concentrations, therefore, offers the best approach for distinguishing the different lithological units and for mapping areas of radiometric enrichment or depletion than with the radioelements (Ohioma et al. 2017). Usually, hydrothermal alteration is identified by high potassium, low thorium while uranium concentration is fairly affected (Ostrovskiy 1975; Ohioma et al. 2017; Hafeez et al. 2015; Dentith and Mudge 2014; Shives et al. 2000). In addition, the zones are often associated with linear and fairly broad magnetic lows (Gunn and Milligan 1997; Dentith and Mudge 2014). We can distinguish meta-felsic and meta-intermediate rocks by high Th/U ratio (Boyle 1979).

Radiogenic heat production

The estimation of radiogenic heat is based on the energy released by the spontaneous disintegration of radioisotopes in geologic formations (Eq. 2) (Rybach 1976; Birch 1954; Alistair et al. 2014).

$$H_R\left(K_c, U_c, Th_c\right) = \rho\left(0.035K_c + 0.097U_c + 0.026Th_c\right). \quad (2)$$

The H_R is the radiogenic heat in $\mu\mathrm{Wm}^{-3}$, ρ is the rock density in $\mathrm{kg/m}^3$ (here taken as the average crustal density), while each of the variables K_c, U_c, Th_c represent the concentration of the measured radioelements namely potassium in percentage (%), uranium, and thorium in part per million (ppm). The expression in Eq. 2 highlights the heat contributed to each of the radioelements to the gross radiogenic heat. The expression shows heat contribution from uranium to be exclusively high. This shows why granitoid-dominated formations with high uranium concentration and fault-controlled hydrothermal zones with exclusively high potassium and possibly uranium concentrations are zones of high radiogenic heat (Alistair et al. 2014; Lee et al. 1984; Manning et al. 2007).

Ground geophysical methods

Electrical resistivity tomography (ERT) method

Two-dimensional electrical resistivity tomography (ERT) employs an array of multiple electrodes to infer the 2-D or 3-D image of subsurface structures and lithological boundaries. The configuration employed in the present study is the dipole–dipole configuration. Measurements were made by manually changing the connectors due to the non-availability of an automatic electrode selector. The survey is based on the injection of a controlled amount of current into the ground through the outer electrodes and then measure the voltage developed from the ground cross-section from the inner electrodes. The voltage is converted to a resistivity value that represents the average ground resistivity at the centre of the inner electrodes. The expansion of the electrode array offset from the central reference point is used to assess the depth to provide models of vertical variations in the ground resistivity. The depth probed increases with wider electrode spacing, resulting in a one-dimensional layered resistivity model. Composite sections are obtained by interpolating between depth probes at a regular interval on a profile (Fig. 2) (Telford et al. 2001). The method has the advantage of defining transitional boundaries between geological formations which may be difficult to detect with other geophysical methods.

Very low-frequency electromagnetic (VLF-EM) method

The very-low-frequency electromagnetic (VLF-EM) method uses high-powered military radio transmitters which operate in the range of 15–30 kHz (Milsom 2003; Reynolds 1997). It measures the induced secondary magnetic field components with two perpendicular induction coils (Abbas et al. 2012).

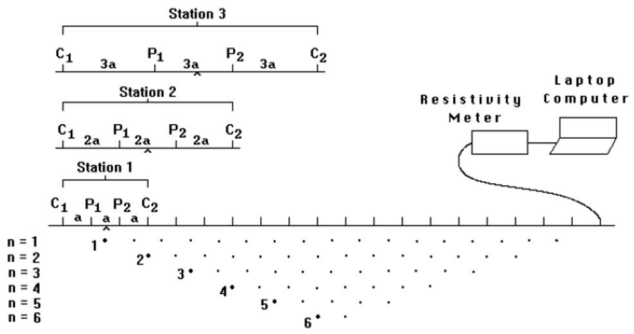

Fig. 2 Array of measurements to create a pseudo section using a computer-controlled multi-electrode survey arrangement (Griffiths and Barker 1993)

In such a case, there is no need for ground contact and, as such allows quick and flexible data acquisition during a field survey.

The local resultant magnetic field H_R is a consequence of the superposition of the primary field H_P and secondary field H_S, for which $H_P >> H_S$. The primary field H_p and the resultant magnetic field H_R depends on space, time, and frequency (Bosch and Müller 2001; Abbas et al. 2012). As a result of the distant field conditions, the primary field, H_p becomes space independence.

A simplified relationship between H_R, H_p and H_S is represented in Eqs. 3, 4, and 5 (these relations are subjected to vector field resolution)

$$H_R = H_S + H_P, \tag{3}$$

$$H_R = \frac{|H_s|e^{i\omega t}}{|H_s|e^{i\alpha}} + |H_p|e^{i\omega t}. \tag{4}$$

The frequency of the transmitter is of the value $f = \frac{\omega}{2\pi}$ and α is the phase shift between primary and secondary magnetic field components (Abbas et al. 2012).

The magnetic field vector components are of the form

$$\begin{pmatrix} 0 \\ H_{Ry} \\ H_{Rz} \end{pmatrix} = \begin{pmatrix} 0 \\ H_{py} \\ 0 \end{pmatrix} + \begin{pmatrix} 0 \\ H_{sy} \\ H_{sz} \end{pmatrix} \tag{5}$$

The results of the VLF-EM method are the in-phase (real/vertical component) and Out-of-phase (imaginary/quadrature/horizontal component) parts of the ratio H_{Ry}/H_{Rz} i.e. (the ratio of the horizontal resultant magnetic field to the vertical resultant magnetic field) (Abbas et al. 2012).

Results and discussion

Aeromagnetic maps

Residual magnetic intensity (RMI) map

The residual magnetic intensity (RMI) map of the study area was derived from the high-resolution aeromagnetic dataset of the study area using Geosoft Oasis Montaj software (Geosoft 1999) (Fig. 3). The original dataset was gridded at 100 m spacing using the minimum curvature gridding algorithm to make the subtle magnetic signatures visible (Brigs 1974). The resulting RMI map highlights magnetic structures with amplitude between -89 nT and 110 nT. The porphyritic granite of the north-northwestern (NNW) parts of the study area shows magnetic signatures with amplitude greater than 70 nT. The banded gneiss and migmatite gneiss

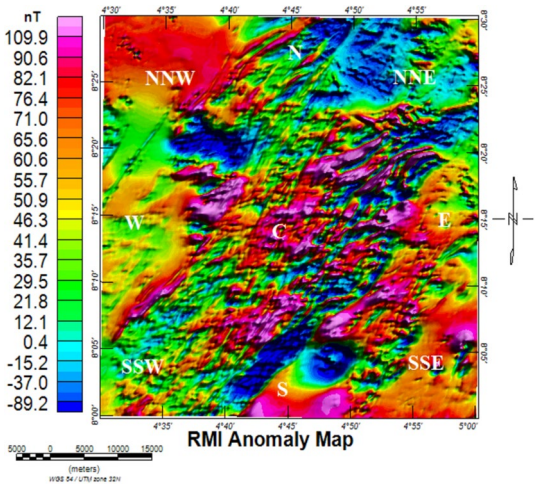

Fig. 3 Residual magnetic intensity (RMI) map of the study area. The parts identified on the map are north–northwest (NNW); north–northeast (NNE); south–southwest (SSW); south–southeast (SSE); central (C); north (N); south (S); East (E) and west (W)

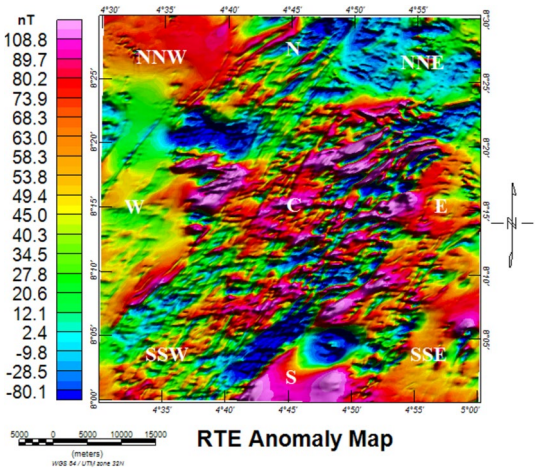

Fig. 4 Reduced to the magnetic equator map (RTE) of the study area

of the central (C) parts exhibit series of linear magnetic anomalies with amplitudes between 60 and 110 nT in specific locations. Similarly, the undifferentiated schist of the south–southeastern (SSE) and the eastern (E) parts exhibit high amplitude magnetic anomalies at places (Fig. 3).

Reduction to the magnetic equator map

The study area falls within the magnetic low latitude of the northern hemisphere with an average inclination, declination, and IGRF intensity of − 8.2°, − 2.7°, and 33,017 nT respectively. The RMI anomaly data of the study area were reduced to the magnetic equator within (Geosoft 1999) software environment (Fig. 4). The purpose is to centre the

amplitudes of the magnetic field on the source bodies. Visual inspection of the RTE map (Fig. 4) shows no appreciable shift in the maxima of the magnetic field when compared with the original data (see Fig. 5). This is because of the proximity of the study area to the magnetic equator. The purpose of the RTE interpretation in this study, therefore, is to justify the use of the RMI map (Fig. 3) for other interpretations. The RMI map (Fig. 3) rather than the RTE map (Fig. 4) was implemented for other interpretations to be sure that the shape, strike and linear extent of the causative bodies, especially the subtle structures, are not compromised.

Horizontal gradient magnitude

The HGM interpretation was implemented to identify the contacts and boundaries of magnetic source bodies. These were identified as magnetic highs or lows in specific locations in the study area. Geologic contacts such as faults, joints, shear zones among others can be pathways through which hydrothermal fluids reach the outer crust (Misra 2000). They, therefore, represent probable locations for targeting hydrothermal mineral deposits related to porphyry, skarn, epithermal, or volcanogenic massive deposits. The special ability of the HGM to distinctly map boundaries of magnetic structures from a set of gridded magnetic data is one of the main standpoints for targeting hydrothermal zones in the study area. The HGM interpretation was derived from the RMI anomaly data using Geosoft Oasis Montaj software (Geosoft 1999) since there was no appreciable transformation with the RTE filter. The purpose is to avoid losing the north–south subtle structures or misrepresent the shapes of the source bodies. The HGM map highlights clusters and pockets of magnetic structures M, with amplitudes between 30 nT/km and 350 nT/km (Fig. 6). Similarly, the map highlights six isolated bodies here labelled H1, H2, H3, H4, H5, and H6 with amplitude between 7 nT/km and 20 nT/km (Fig. 6). Considering the low amplitude magnetic signature of the H-zones (Black outlines in Fig. 6), these zones, therefore, represent the initial suspected hydrothermal alteration zones to be investigated further. The magnetic structures of the M-zones (white outlines in Fig. 6) may be interpreted as many

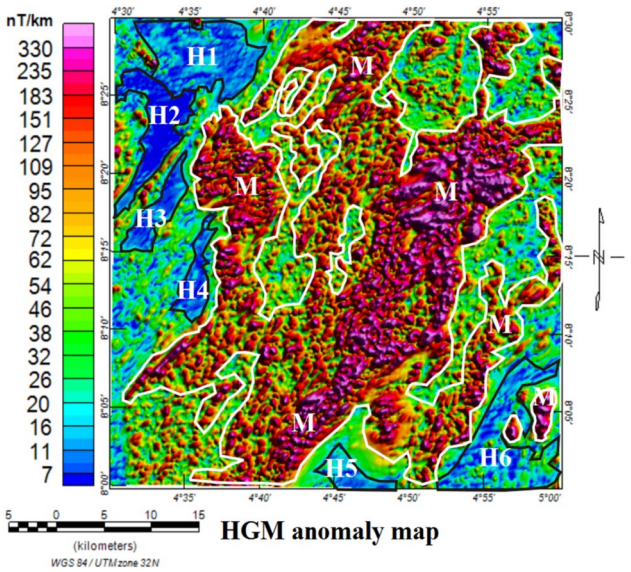

Fig. 6 Horizontal gradient magnitude (HGM) map showing the study area divided into magnetic (M) and probably non-magnetic hydrothermal zones (H)

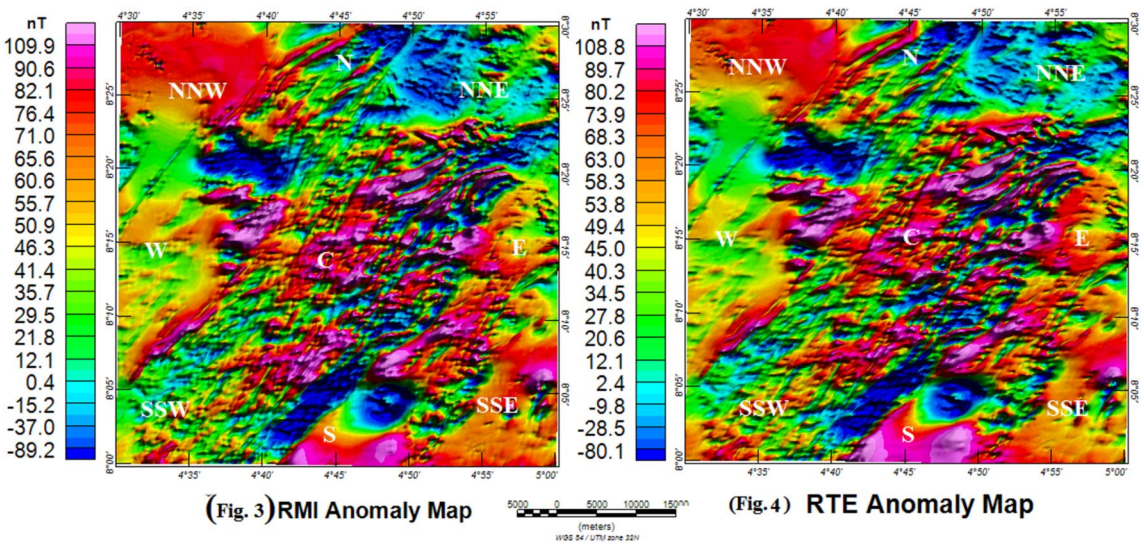

Fig. 5 Comparison of RMI (Fig. 3) and RTE (Fig. 4)

Pan-African igneous rocks rich in magnetic minerals within the older migmatite-gneiss complex.

Aeroradiometric maps

Radiometric concentration maps

The radiometric maps comprising the Potassium (K), Thorium (eTh), and Uranium (eU) were derived from the aeroradiometric data of the same coverage as the aeromagnetic data using Geosoft Oasis Montaj software (Geosoft 1999) (Fig. 7a–c respectively). The data were gridded at 100 m spacing using the Minimum Curvature gridding algorithm to make the subtle radiometric signatures visible (Brigs 1974). The potassium map shows the porphyroblastic gneiss and porphyritic granite formation in the north northwestern part of the study area and a small location in the southern part to exhibit high potassium concentration (Fig. 7a) while each of the thorium and uranium maps shows the undifferentiated gneiss and migmatite gneiss of the south southeastern part of the study area to exhibit a fairly high concentration of the radioelement (Figs. 7b and c respectively).

Radiometric ratio

The ratio of potassium concentration in % and thorium concentration in ppm (Fig. 8a) was evaluated using Geosoft Oasis Montaj software (Geosoft 1999) to identify areas of preferential potassium enrichment. The result obtained shows a very large portion of the north-northwestern segment to be preferentially rich in potassium (yellow outlines in Fig. 8a). To further narrow the study area to the most

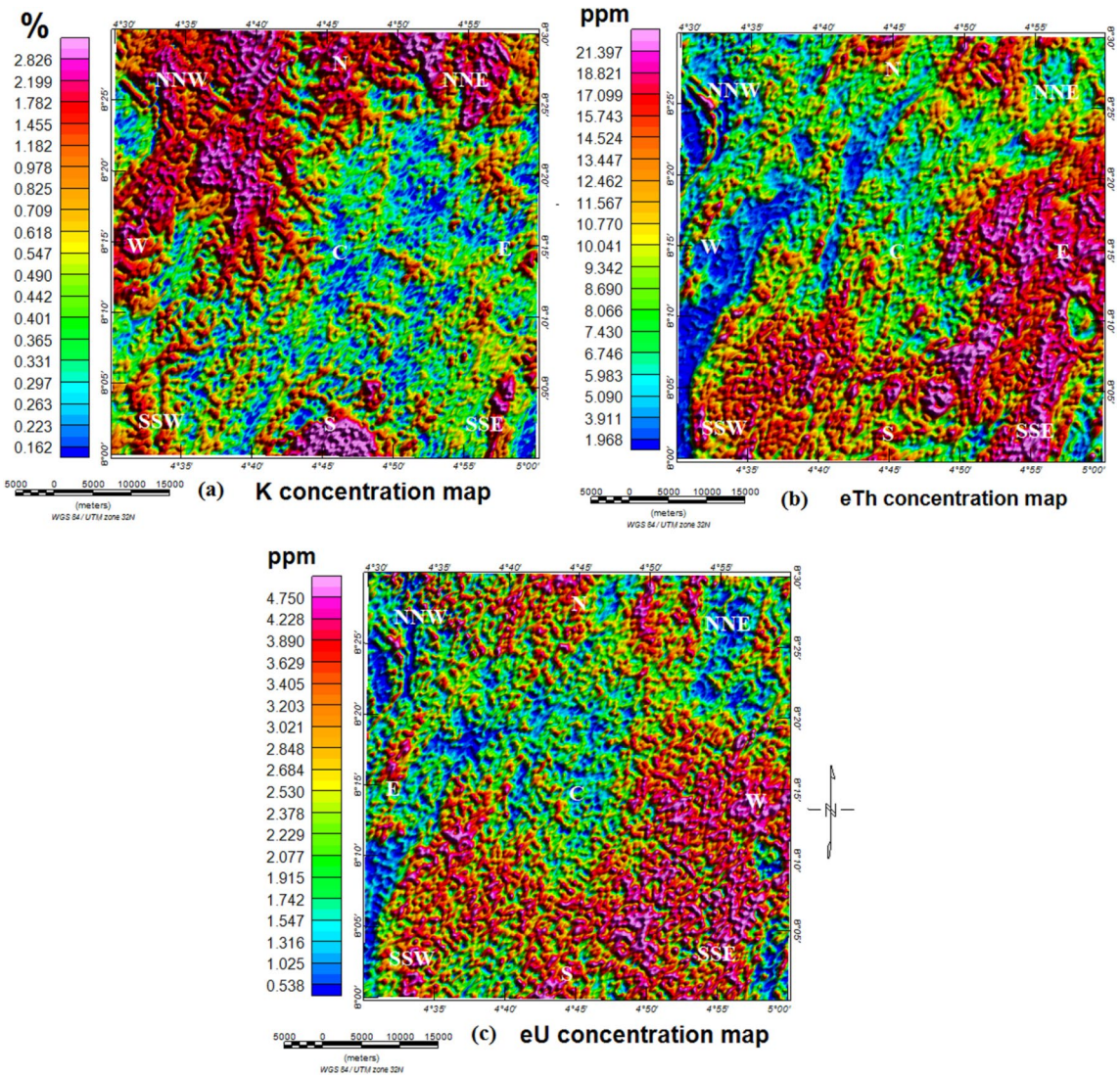

Fig. 7 **a** Potassium concentration map; **b** thorium concentration map; **c** uranium concentration map

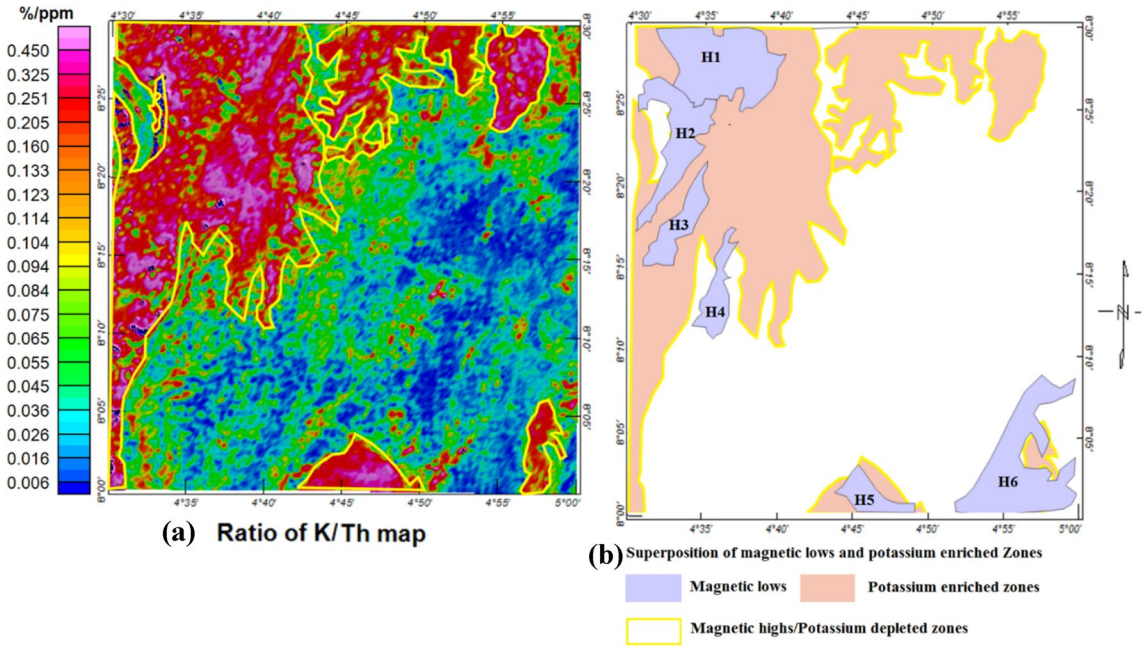

Fig. 8 **a** Map showing zones of potassium enrichment derived from K/Th ratio (outlined in yellow); **b** an overlay of suspected hydrothermal zones from HGM interpretation (see Fig. 7) and the potassium-rich zones from the K/Th map (**a**)

probable hydrothermal alteration zones, the K/Th map (Fig. 8a) and the HGM anomaly map (see Fig. 6) of the study area were extracted for correlation. The suspected demagnetized hydrothermal alteration zones H1, H2, H3, H4, H5 and H6 from the HGM map (black outlines in Fig. 6) and the potassium-rich zones (yellow outlines in Fig. 8a) were extracted and superimposed (Fig. 8b). Visual inspection of Fig. 8b shows H1, H2, H3, H5, and parts of H4 and H6 to fall within high potassium concentration areas of Fig. 8a. The potassium-depleted areas from K/Th map (Fig. 8a) also coincided with the magnetic highs from the HGM map (see Fig. 6). The result shows the north-northwestern parts of the study area to be relatively rich in potassium radioelement (Fig. 8a) and host three of the suspected hydrothermal alteration zones (H1, H2 and H3). Considering the result in Fig. 8b and the local geologic data (see Fig. 1b), it is possible that zones H1, H2 and H5 are within the porphyritic granite of the study area. This means that one can easily assume that the high potassium and low thorium concentrations associated with the H1, H2 and H5 may have resulted from the local geologic formation. However, the low amplitude magnetic signatures exhibit by these structures (H1, H2 and H5) is another reason to still believe that they may be alteration zones, probably, hosted by porphyric granite. Similarly, the geolocation of H3 regarding the local geologic data (see Fig. 1b) equally showed that zone H3 is likely hosted within geological contact between porphyroblastic gneiss and banded gneiss. This implies that, the high potassium and low thorium concentration may have resulted from the hydrothermal alteration of the affected geologic formation. The H4 falls within the silicified quartz-schist belt in parts of the study area. The low amplitude and high potassium concentration in this structure may equally be attributed to the rock-type hosting the structure.

Radiogenic heat

The fact that fault-controlled hydrothermal alteration zones can exhibit high radiogenic heat as a result of potassium and uranium concentrating in faults or joints allows us to further distinguish the most probable hydrothermal alteration zones out of the six zones identified. The result obtained after applying the radiogenic heat equation (Eq. 2) shows the hydrothermal alteration zone H3 to exhibit high radiogenic heat compared to the other suspected alteration zones H1, H2, H4, H5 and H6 (Fig. 9). This result allowed us to focus more on zone H3. The widths and length of the H3 zone were measured to see the possibility of detecting it with airborne survey (see Fig. 8b). Dickson and Scott (1997) suggested a detectable minimum width of 1 km for the hydrothermal alteration zone. However, the average width and length of 5 km and 30 km respectively obtained for H3 is well above the minimum detectable size. The result of the radiogenic heat production showed radiogenic heat well above 2.7 μWm^{-3} for the H3 zone (Fig. 9). The zones H5 and H6 with similar high radiogenic heat may be attributed to the undifferentiated schist in affected areas (see the south-southeastern part of Fig. 9). In contrast, the radiogenic

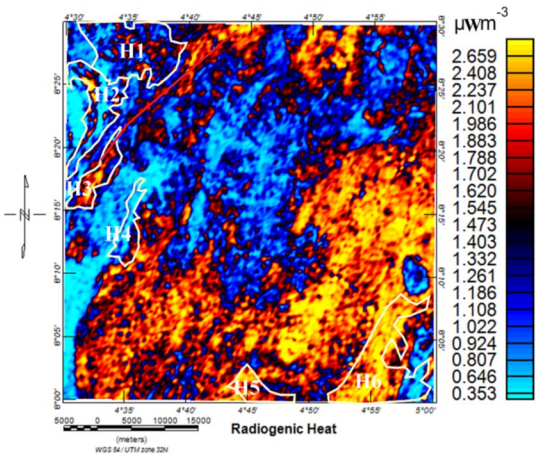

Fig. 9 An overlay of suspected hydrothermal zones from HGM interpretation on the radiogenic heat map

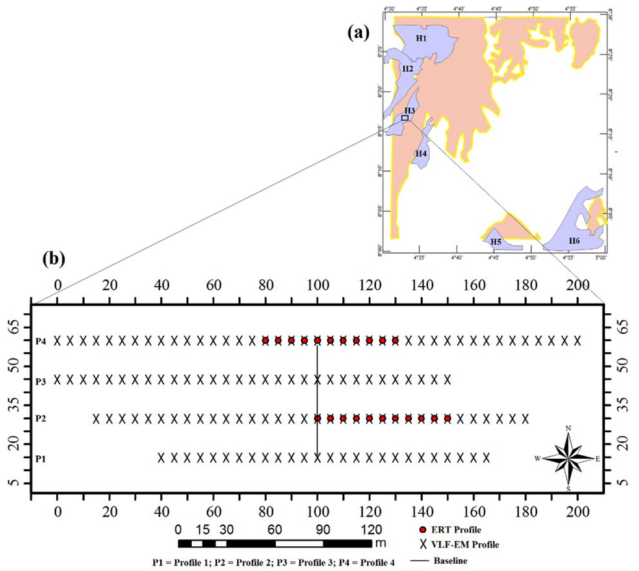

Fig. 10 **a** Structural map of airborne geophysical surveys showing suspected hydrothermal alteration zones namely H1, H2, H3, H4, H5 and H6; **b** base map of the ground geophysical survey showing ERT and VLF-EM profiles from where the ground geophysical data were acquired in part of H3

heat for zones H1, H2 and H4 is nowhere greater than 0.4 μWm^{-3}. Visual inspection of the radiogenic heat map (Fig. 9) shows a possibility of the radiogenic heat through zone H3 extending beyond H3 (see the red line in Fig. 9). This extension suggests that a crustal opening, probably a major fault is responsible for the alteration zone H3.

Ground geophysical surveys

Considering the results of each of the airborne geophysical surveys namely HGM, K/Th, especially the radiogenic heat (see Figs. 6, 8a and 9 accordingly), the suspected hydrothermal alteration zones H3 was singled out for ground geophysical surveys to establish the results of the airborne geophysical surveys and to understand the mineral prospect of the H3 structure. Two ground geophysical surveys namely electrical resistivity tomography (ERT) and very-low-frequency electromagnetic (VLF-EM) methods were conducted in part of zone H3. Figure 10a shows zone H3 in the north–northwestern part of the study area, while Fig. 10b shows the ERT and VLF-EM profiles in part of the hydrothermal zone H3 where each of the data was acquired. Both profiles cut the suspected structure in east–west traverses. The ERT profiles are shown by the red circle while the VLF-EM profiles are represented by the transect symbol (Fig. 10b).

Electrical resistivity tomography (ERT)

The ERT survey was conducted in part of the hydrothermal zone H3 to provide additional insights into the structural disposition of the complex formation. An array of dipole–dipole electrodes was established in an east–west traverse and measurements were made for a profile length of 50 m. Two tomography sections A–A′ and B–B′ (Fig. 11a and b) were obtained using RES2DINV software (Geotomo 2000–2007; 2021). The 2-D sections present the subsurface electrical resistivity distribution up to an approximate depth of 8.5 m in parts of H3. The suspected hydrothermal alteration zone was identified as a slightly deformed and fairly homogenous section 5 m below fairly weathered heterogeneous geological sections (Fig. 11a and b). The suspected alteration segments of the ERT pseudo sections (Fig. 11a and b) exhibit resistivity values between 900 and 1200 Ωm. These high resistivity values may be attributed to the destruction of magnetic minerals in the affected rock(s) as a result of hydrothermal fluids infiltration. The results of the ERT survey, though able to delineate the lithological boundaries in the affected formation, could not provide further evidence for the infiltration of the hydrothermal fluids or possible hosts of economic deposits.

Very low-frequency electromagnetic (VLF-EM)

The VLF-Em survey was undertaken in part of the hydrothermal alteration zone H3 in search of structures and conduits of hydrothermal fluids. Four east–west profiles were established and measurements were made at a very close interval of 5 m. The raw real data acquired for each profile were interpreted using Karous–Hjelt and Fraser filters (Karous Hjelt 1983; Fraser 1969) within KHFFILT software (Markku 2004). The Fraser outputs namely filter real and filter imaginary were plotted over the Karous–Hjelt 2-D pseudo-sections (Fig. 12a–d). The positive peaks of the filter

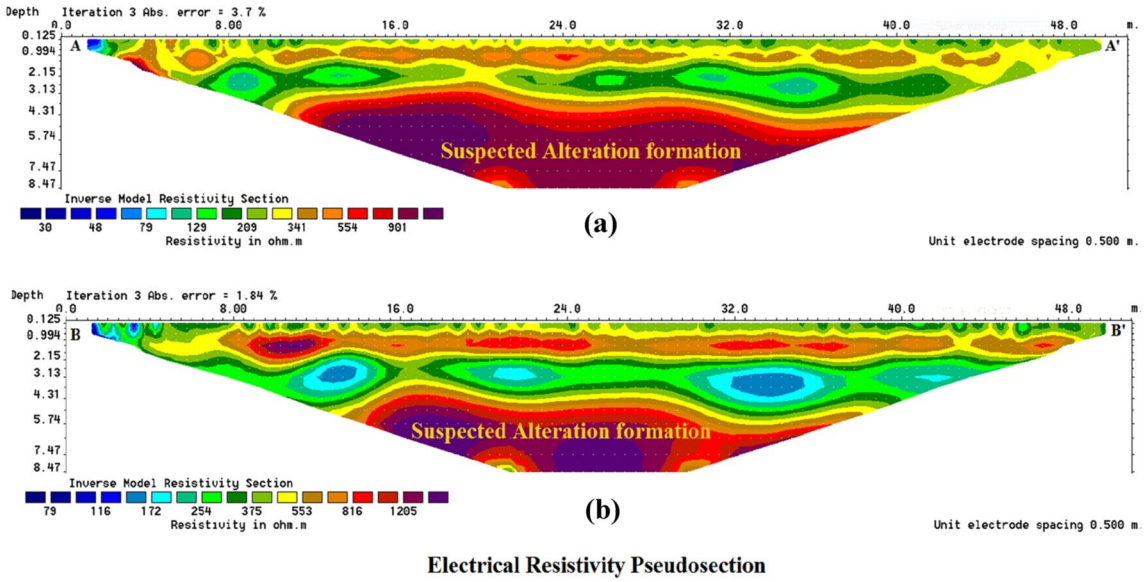

Fig. 11 **a** 2-D resistivity section A–A′, **b** 2-D resistivity section B–B′

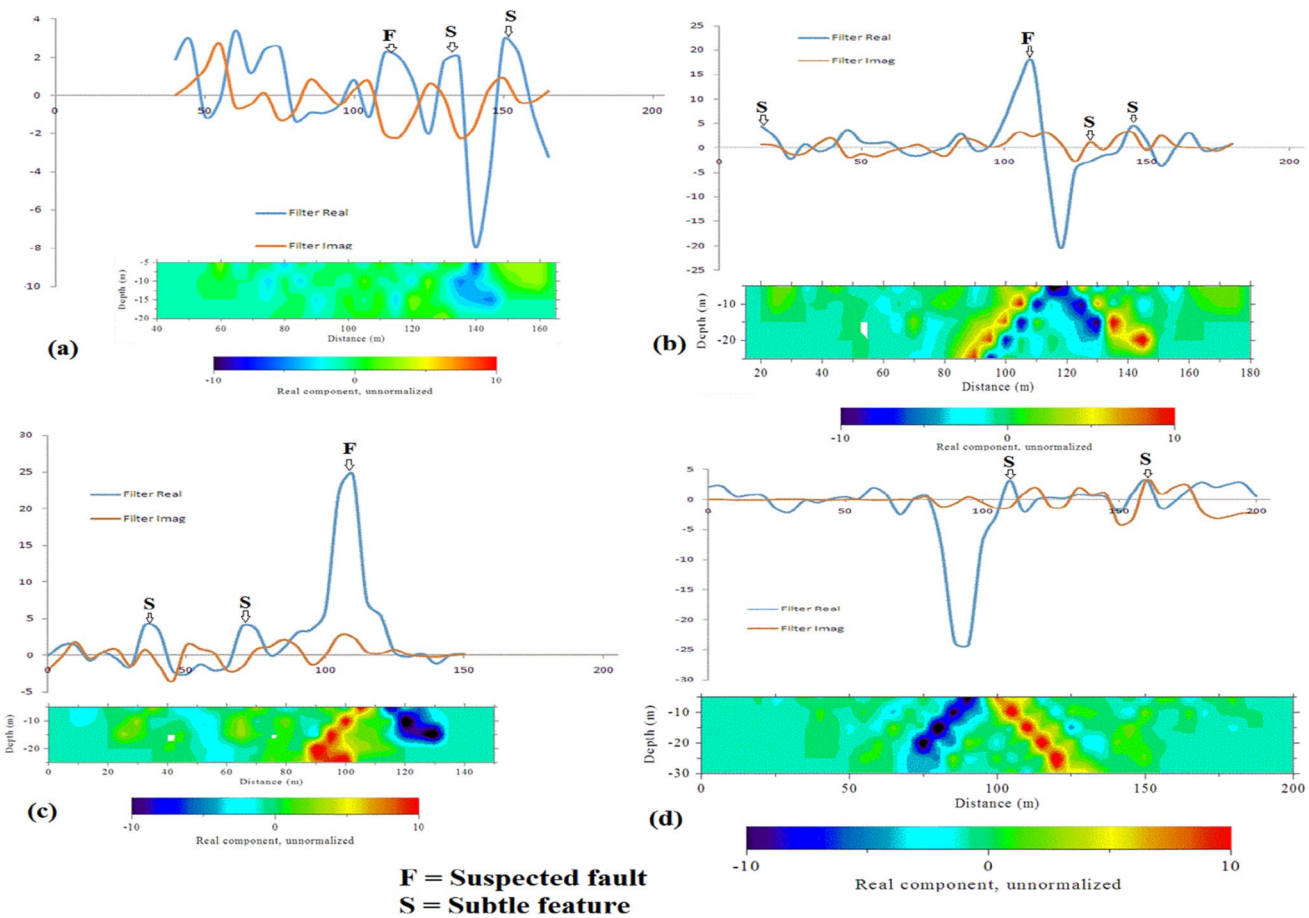

Fig. 12 VLF filtered real and filtered imaginary curves plotted over the 2-D section. The profiles shown are **a** profile one, **b** profile two, **c** profile three, **d** profile four

real from the Fraser filter coincided with the low resistivity parts of the Karous–Hjelt pseudo-sections indicating weak zones such as faults or joints and are identified as "F" in affected locations (Fig. 12a–d). Similarly, some small positive peaks were equally identified on the plots and denoted as "S" (Fig. 12a–d). They represent subtle signatures that may have resulted from the crustal structures hosting conductive minerals such as sulfide minerals which can be one of the associated minerals in the structures hosting economic deposits. The faults/joints identified as "F" from the VLF-EM interpretations (Fig. 12a–d) may represent the main plumbing system through which hydrothermal fluids were focused into subsidiary fractures and other structures for which the interaction of the fluids with suitable wall rocks caused mineral precipitation. Furthermore, the negative peaks also coincided with the high resistivity parts of the VLF-EM pseudo-section (Fig. 12a–d). These structures may represent wall rocks in affected parts of the alteration zone H3 (see Fig. 12a–d).

Conclusion

The integration of four geophysical methods namely magnetic, radiometric, electrical resistivity tomography (ERT) and very-low-frequency electromagnetic (VLF-EM) methods in this study provides new insights for effectively mapping hydrothermal alteration zones especially in an area where the alteration signatures are completely concealed below the surface. The results presented in this study (Figs. 4, 5, 6, 7, 8, 9, 10, 11, 12) showed that hydrothermal alteration zone H3, from the list of the other six zones namely H1, H2, H4, H5 and H6, showed positive prospects for hydrothermal alteration zone. These features include but are not limited to the magnetic lows that suggest demagnetization of the host structures (Fig. 6); high potassium concentration accompanied by thorium depletion (Fig. 8a); high radiogenic heat that provides evidence for its geothermal property (Fig. 9); moderately high electrical resistivity that implied a non-conductive or possibly a demagnetized formation (Fig. 11a and b); evidence of weak zones in specific parts that suggest fault/fractures through which hydrothermal fluids may have been focused in subsidiary structures for subsequent minerals precipitation in wall-rocks (Fig. 12a–d). Finally, the measured average width of 5 km and length of about 30 km for the hydrothermal alteration zone H3 provide additional evidence for its detection from the surface.

Declarations

Conflict of interest The authors declare that they have no known competing financial interests or personal relationships that could appear to have influenced the work reported in this paper.

References

Abbas MA, Mohamed AK, Usman M, Fernando MS, Hany AM, Ahmed L, Mamdouh S, El-Said AR (2012) The implementation of a multi-task geophysical survey to locate Cleopatra Tomb at Tap-Osiris Magna, Borg El-Arab, Alexandria, Egypt Phase II. J Astro Geophy 1:1–11

Adebiyi LS, Fatoba JO, Salawu NB, Dopamu KO, Abdulraheem TY, Obaseki OS, Olasunkanmi NK, Adediran SO (2020) Analysis of aeromagnetic data: application to early—late Cretaceous events in parts of Lower Benue trough, Southern Nigeria. J Appl Geophys 178:1–18

Ajibade AC, Woakes M, Rahaman MA (1987) Proterozoic crustal development in the Pan-African regime of Nigeria. In: Kröner A (ed) Proterozoic lithospheric evolution. American Geophysical Union, Washinton DC (USA, pp 259–271)

Airo ML (2002) Aeromagnetic and aeroradiometric response to hydrothermal alteration. Surv Geophys 23(4):273–302. https://doi.org/10.1023/A:1015556614694

Alistair TM, Thomas LH, Paul LY, David CWS, Alan JC (2014) Gamma-ray spectrometer in geothermal exploration: state of the art techniques. Energies 7:4757–4780

Birch F (1954) Heat from radioactivity. Nuclear geology. Wiley, New York, pp 148–174

Blakely RJ (1995) Potential theory in gravity and magnetic applications. Potential theory in gravity and magnetic applications. Cambridge University Press. https://doi.org/10.1017/cbo9780511549816

Bosch FP, Muller I (2001) Continuous gradient VLF measurements: a new possibility for high resolution mapping of karst structures. Tech Rep EAGE First Break 19–6:343–350

Boyle RW (1979) The geochemistry of gold and its deposits. Geol Surv Can Bull 280:584

Brigs IC (1974) Machine contouring using minimum curvature. Geophysics 39(1):39–48

Burnham CW (1979) Magmas and hydrothermal fluids. In: Bames HL (ed) Geochemistry of hydrothermal ore deposits, 2nd edn. Wiley, New York, pp 71–136

Burnham CW (1981) Physicochemical constraints on porphyry mineralization. In: Dickinson RW, Payne WD (eds) Relations of tectonics to ore deposits in the southern Cordillera, vol 14. Arizona Geol Soc Digest, pp 71–77

Burnham CW (1997) Magmas and hydrothermal fluids. In: Barnes HL (ed) Geochemistry of hydrothermal ore deposits, 3rd edn. Wiley, New York, pp 63–123

Burnham CW, Ohmoto H (1980) Late-stage processes of felsic magmatism. In: Ishihara S, Takenouchi S (eds) Granitic magmatism and related mineralization, vol 8. Mining Geol Spec, pp 1–11

Cordell L, Grauch VJS (1982) Mapping basement magnetization zones from aeromagnetic data in the San Juan Basin, New Mexico: 52nd Annual International Meeting, SEG, Expanded Abstracts, pp 246–247

Dada SS (2008) Proterozoic evolution of the Nigeria–Boborema province. In: Pankhurst RJ, Trouw RAJ, de Brito Neves BB, deWit MJ (eds) West Gondwana: precenozoic correlations across the south Atlantic region, 294. Geological Society, London, pp 121–136. https://doi.org/10.1144/sp294.7. Special Publications

Dentith M, Mudge S (2014) Geophysics for the mineral exploration geoscientist. AusIMM Bull. https://doi.org/10.1017/cbo9781139024358

Dickson BL, Scott KM (1997) Interpretation of aerial gamma-ray surveys - adding the geochemical factors. J Aust Geol Geophys 17(2):187–200

Eilu PK, Mathison CI, Groves DI, Allardyce WJ (1999) Atlas of alteration assemblages, styles and zoning in orogenic lode-gold deposits in a variety of host rock and metamorphic settings. UWA Ext, Univ West Aust Publ, p 30

Eldosouky AM, Abdelkareem M, Elkhateeb SO (2017) Integration of remote sensing and aeromagnetic data for mapping structural features and hydrothermal alteration zones in Wadi Allaqi area, South Eastern Desert of Egypt. J Afr Earth Sci 130:28–37

Fedi M, Florio G (2001) Detection of potential fields source boundaries by the enhanced horizontal derivative method. Geophys Prospect 49:40–58

Fraser DC (1969) Contouring of VLF-EM data. Geophysics 34(6):958–967. https://doi.org/10.1190/1.144006

Geosoft (1999) Oasis montaj data processing and analysis (DPA) systems for earth science applications. Geosoft Incorporated, West Toronto, p 576

Geotomo (2021) Res2DInv software available at: https://www.aarhusgeosoftware.dk/res2dinv

Griffiths DH, Barker RD (1993) Two-dimensional resistivity imaging and modelling in areas of complex geology. J Appl Geophys 29(3–4):211–226. https://doi.org/10.1016/0926-9851(93)90005-J

Guilbert JM, Park CF (1986) The geology of ore deposits. Freeman, New York, San Francisco

Gunn PJ, Maidment D, Milligan PR (1997) Interpreting aeromagnetic data in areas of limited outcrop. J Aust Geol Geophys 17(2):175–185

Hafeez THA, Youssef MAS, Mohamed WH (2015) Utilization of airborne gamma ray spectrometric data for geological mapping and radioactive mineral exploration of Gabel Umm Tineidba area, south eastern desert, Egypt. World J Eng 12:149–160. https://doi.org/10.1260/1708-5284.12.2.149

Holden EJ, Fu SC, Kovesi P, Dentith M, Bourne B, Hope M (2011) Automatic identification of responses from porphyry intrusive systems within magnetic data using image analysis. J Appl Geophys 74(4):255–262. https://doi.org/10.1016/j.jappgeo.2011.06.016

Holland HD (1972) Granites, solutions and base metal deposits. Econ Geol 67:281–301

Karous M, Hjelt SE (1983) Linear filtering of VLF dip-angle measurements. Geophys Prospect 31(5):782–794. https://doi.org/10.1111/j.1365-2478.1983.tb01085.x

Lambert IB, Sato T (1974) The kuroko and associated deposits of Japan: a review of their features and metallogenesis. Econ Geol 69:1215–1236

Lawal TO (2020) Integrated aeromagnetic and aeroradiometric data for delineating lithologies, structures, and hydrothermal alteration zones in part of southwestern Nigeria. Arab J Geosci 13:775. https://doi.org/10.1007/s12517-020-05743-7

Lee M, Wheildon J, Webb P, Brown G, Rolling K, Crook C, Smith I, King G, Thomas-Betts A (1984) Hot dry rocks prospects in caledomian granites: evaluation of results from the bgs-ic-ou research programme. Keyworth UK investigation of the geothermal potential of the UK. British Geological Survey, pp 1981–1984

Lentz DR (1994) Alteration and alteration processes associated with ore-forming systems. (ed) Short Course Notes 11, Geol Ass Can, Waterloo, pp 467

Manning D, Younger P, Smith F, Jones J, Dufton D, Diskin S (2007) A deep geothermal exploration well at Eastgate, Weardale, UK: a novel exploration concept for low-enthalpy resources. J Geol Soc 2:371–382

Markku P (2004): KHFFILT Software available at: https://sites.google.com/view/markkussoftware/electric-and-em-software/khffilt?authuser=0

MacLeod LN, Jones K, Dai TF (1993) 3-D analytic signal in the interpretation of total magnetic field data at low magnetic latitudes. Explorat Geophy 24:679–688

Misra KC (2000) Understanding mineral deposits. Springer-Science + Business Media, B.V. ebook, Vol. 1.

Meyer C, Hemley JJ (1967) Wall rock alteration. In: Barnes HL (ed) Geochemistry of hydrothermal ore deposits, 1st edn. Holt Rinehart & Winston, New York, pp 166–235

Mielke PB, Greg, Sass I (2014) Predicting the effect of hydrothermal alteration on rock properties. In: Proceedings 36th New Zealand Geothermal Workshop

Milsom J (2003) Field geophysics: the geological field guide series. Willey

Moritz M (2009) Magnetic anomaly interpretation of the north German Basin: results from depth estimation and 2D-Modeling. Bachelor of Science Thesis, Department of Earth and Space Sciences, Jacobs University Bremen, Bremen, Germany

Nabighian MN, Grauch VJS, Hansen RO, LaFehr TR, Li Y, Peirce JW, Phillips JD, Ruder ME (2005) The historical development of the magnetic method in exploration. Geophysics 70(6):33–61

Nigerian Geological Survey Agency (2006) Nationwide Geological Map. NGSA, 31 Shetima Munguno Crescent, Utako, Abuja, Nigeria

Nigerian Geological Survey Agency (2007) Nationwide Aeromagnetic Data. NGSA, 31 Shetima Munguno Crescent, Utako, Abuja, Nigeria

Ohioma JO, Ezomo FO, Akinsunmade A (2017) Delineation of hydrothermally altered zones that favour gold mineralization in Isanlu Area, Nigeria using aeroradiomatric data. Int Ann Sci 2(1):20–27

Ostrvskiy EA (1975) Antagonism of radioactive elements in wall rock alteration fields and its use in aerogamma spectrometric prospecting. Int Geol Rev 17(4):461–468

Phillips JD (2000) Locating magnetic contacts: a comparison of the horizontal gradient, analytic signal, and local wavenumber methods. In: 70th Meeting, Calgary, Society of Exploration Geophysicists, Expanded Abstracts with Biographies, 2000 Technical Program, 1:402–405

Pirajno F (1992) Hydrothermal mineral deposits—principles and fundamental concepts for the exploration geologist. Springer-Verlag

Reynolds JM (1997) An introduction to applied and environmental geophysics. Wiley

Rybach L (1976) Radioactive heat production: a physical property determined by the chemistry of rocks. In: Stems RGJ (ed) The physics and chemistry of minerals and rock. Wiley-Interscienc, New York, pp 309–318

Salawu NS, Olatunji S, Adebiyi LS, Olasunkanmi N, Dada SS (2019) Edge detection and magnetic basement depth of Danko area, northwest Nigeria from low-latitude aeromagnetic anomaly data. Springer Nat J 1:1–16

Salawu NB, Fatoba JO, Adebiyi LS, Ajadi J, Saleh A, Dada SS (2020) Aeromagnetic and remote sensing evidence for the structural framework of the middle Niger and Sokoto basins, Nigeria. Physics of the Earth and Planetary Interiors, 309. https://doi.org/10.1016/j.pepi.2020.106593

Shives R, Charbonneau B, Ford K (2000) The detection of potassic alteration by gamma-ray spectrometry-recognition of alteration related to mineralization. Geophysics 65(6):2001–2011

Smith LB, Davies GR (2006) Structurally controlled hydrothermal alteration of carbonate reservoirs: introduction. Am Assoc Petrol Geol Bull. https://doi.org/10.1306/intro901106

Telford WM, Geldart LP, Sheriff RE (2001) Applied geophysics. Cambridge University Press

Thieblemont D (ed) (2016) Geological map of African at 1: 10M scale. CGMW-BRGM

Thompson AJB, Thompson JFH (eds) (1996) Atlas of alteration—a field and petrographic guide to hydrothermal alteration minerals. Min Depos Div, Geol Ass Can, Mem Univ Newfoundland, St John's Newfoundland

Verduzco B, Fairhead JD, Green CM, Mackenzie C (2004) New insights into magnetic derivatives for structural mapping. The Lead Edge 23:116–119

White RW, Powell R, Phillips GN (2003) A mineral equilibria study of the hydrothermal alteration in mafic greenschist facies rocks at Kalgoorlie, Western Australia. J Metamorph Geol 21(5):455–468. https://doi.org/10.1046/j.1525-1314.2003.00454.x

Terms and Conditions

Springer Nature journal content, brought to you courtesy of Springer Nature Customer Service Center GmbH (“Springer Nature”).
Springer Nature supports a reasonable amount of sharing of research papers by authors, subscribers and authorised users (“Users”), for small-scale personal, non-commercial use provided that all copyright, trade and service marks and other proprietary notices are maintained. By accessing, sharing, receiving or otherwise using the Springer Nature journal content you agree to these terms of use (“Terms”). For these purposes, Springer Nature considers academic use (by researchers and students) to be non-commercial.
These Terms are supplementary and will apply in addition to any applicable website terms and conditions, a relevant site licence or a personal subscription. These Terms will prevail over any conflict or ambiguity with regards to the relevant terms, a site licence or a personal subscription (to the extent of the conflict or ambiguity only). For Creative Commons-licensed articles, the terms of the Creative Commons license used will apply.
We collect and use personal data to provide access to the Springer Nature journal content. We may also use these personal data internally within ResearchGate and Springer Nature and as agreed share it, in an anonymised way, for purposes of tracking, analysis and reporting. We will not otherwise disclose your personal data outside the ResearchGate or the Springer Nature group of companies unless we have your permission as detailed in the Privacy Policy.
While Users may use the Springer Nature journal content for small scale, personal non-commercial use, it is important to note that Users may not:

1. use such content for the purpose of providing other users with access on a regular or large scale basis or as a means to circumvent access control;
2. use such content where to do so would be considered a criminal or statutory offence in any jurisdiction, or gives rise to civil liability, or is otherwise unlawful;
3. falsely or misleadingly imply or suggest endorsement, approval , sponsorship, or association unless explicitly agreed to by Springer Nature in writing;
4. use bots or other automated methods to access the content or redirect messages
5. override any security feature or exclusionary protocol; or
6. share the content in order to create substitute for Springer Nature products or services or a systematic database of Springer Nature journal content.

In line with the restriction against commercial use, Springer Nature does not permit the creation of a product or service that creates revenue, royalties, rent or income from our content or its inclusion as part of a paid for service or for other commercial gain. Springer Nature journal content cannot be used for inter-library loans and librarians may not upload Springer Nature journal content on a large scale into their, or any other, institutional repository.
These terms of use are reviewed regularly and may be amended at any time. Springer Nature is not obligated to publish any information or content on this website and may remove it or features or functionality at our sole discretion, at any time with or without notice. Springer Nature may revoke this licence to you at any time and remove access to any copies of the Springer Nature journal content which have been saved.
To the fullest extent permitted by law, Springer Nature makes no warranties, representations or guarantees to Users, either express or implied with respect to the Springer nature journal content and all parties disclaim and waive any implied warranties or warranties imposed by law, including merchantability or fitness for any particular purpose.
Please note that these rights do not automatically extend to content, data or other material published by Springer Nature that may be licensed from third parties.
If you would like to use or distribute our Springer Nature journal content to a wider audience or on a regular basis or in any other manner not expressly permitted by these Terms, please contact Springer Nature at

onlineservice@springernature.com